



Ratcheting, wrinkling and collapse of tubes under axial cycling

Rong Jiao, Stelios Kyriakides*

Research Center for Mechanics of Solids, Structures & Materials, WRW 110, C0600, The University of Texas at Austin, Austin, TX 78712, USA

ARTICLE INFO

Article history:

Received 21 January 2009

Received in revised form 10 March 2009

Available online 1 April 2009

Keywords:

Ratcheting

Wrinkling

Collapse

Cyclic loading

Circular tubes

ABSTRACT

Circular tubes compressed into the plastic range first buckle into axisymmetric wrinkling modes. Initially the wrinkle amplitude grows with increasing load. The wrinkles gradually induce a reduction in axial rigidity eventually leading to a limit load instability followed by collapse. The two instabilities can be separated by strain levels of a few percent. This work investigates whether a tube that develops small amplitude wrinkles can be subsequently collapsed by persistent cycling. The problem is first investigated experimentally using SAF 2507 super-duplex steel tubes with D/t of 28.5. The tubes are first compressed to strain levels high enough for mild wrinkles to form; they are then cycled axially under stress control about a compressive mean stress. This type of cycling usually results in material ratcheting or accumulation of compressive strain; here it is accompanied by accumulation of structural damage due to the growth of the amplitude of the initial wrinkles. The tube average strain initially grows nearly linearly with the number of cycles, but as a critical value of wrinkle amplitude is approached, wrinkling localizes, the rate of ratcheting grows exponentially and the tube collapses. The rate of ratcheting and the number of cycles to failure depend on the initial compressive pre-strain and on the amplitude of the stress cycles. However, collapse was found to occur when the accumulated average strain reaches the value at which the tube localizes under monotonic compression. A custom shell model of the tube with initial axisymmetric imperfections, coupled to a cyclic plasticity model, are presented and used to simulate the series of experiments performed successfully. A sensitivity study of the formulation to the imperfections and to key constitutive model parameters is then performed.

© 2009 Elsevier Ltd. All rights reserved.

1. Introduction

The problem of plastic buckling of circular tubes and pipes with relatively low diameter-to-thickness ratios due to axial loading has had a life of at least fifty years and consequently can be categorized as “classical.” Unlike elastic shell buckling in which collapse is sudden, catastrophic, and very imperfection sensitive, failure due to plastic buckling involves a sequence of instabilities that can be separated by average strains of 1–5% (e.g., see experiments by Lee (1962); Batterman (1965); Bardi and Kyriakides (2006); Kyriakides and Corona (2007)). The behavior is summarized schematically in the axial stress-shortening ($\sigma_x - \delta_x/L$) response of a long tube shown in Fig. 1. The tube first deforms uniformly into the plastic range of the material (OA). At a strain level indicated by “↓” on the response the tube buckles into an axisymmetric wrinkling mode, henceforth called *wrinkling*. The wrinkle amplitude is initially small but with further compression gradually grows (AB). The growth of the wrinkles causes a corresponding reduction in the axial rigidity of the shell and eventually at B a limit load is at-

tained (indicated by “^”). Beyond this point, deformation localizes usually in one axisymmetric lobe while the load decreases (BC); in other words the structure starts to collapse but the response can be tracked under displacement controlled loading. Thus, the load maximum is considered as the limit state of the structure. In the case shown the onset of wrinkling and the limit state are separated by an average strain of about 3%. For somewhat thinner shells, following some axisymmetric wrinkling an instability involving a switch to a non-axisymmetric mode with 2, 3 or more circumferential waves can develop. The new buckling mode tends to lead to its own load maximum and localization as shown in Fig. 3 of Bardi and Kyriakides (2006) (for analytical efforts at the problem see Gellin (1979); Bushnell (1982); Tvergaard (1983a,b); Yun and Kyriakides (1990); Bardi et al. (2006); Kyriakides and Corona (2007)).

The present study is concerned with the following related cyclic loading problem. Consider a cylindrical shell that has been initially plastically compressed to some extent and subsequently undergoes cyclic loading either purely axial or combined with a second constant load such as internal pressure. It is well known that cyclic loading of a plasticized material even applying relatively small amplitude cycles can cause strain ratcheting (e.g., see Bairstow

* Corresponding author.

E-mail address: skk@mail.utexas.edu (S. Kyriakides).

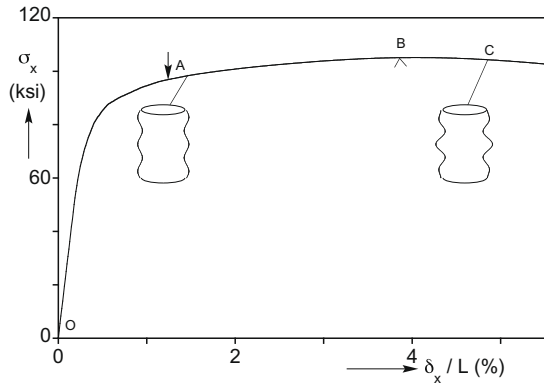


Fig. 1. Typical stress-shortening response from a compression test of an inelastic circular cylinder. Shown are the onset of wrinkling (A) followed by axisymmetric collapse (B) and localization (C).

(1911); Benham (1961); Coffin (1964); Morrow (1965); Sandor (1972); Pilo et al. (1979); Hassan and Kyriakides (1992); Hassan et al. (1992)). The question that arises then is: how does strain ratcheting interact with prevalent plastic structural instabilities such as for instance axial wrinkling.

Structural degradation under cyclic loadings has received some attention in the literature. For example, Kyriakides and Shaw (1987); Corona and Kyriakides (1991) and Chang and Pan (2009) reported degradation of tubes under cyclic bending in the form of accumulated ovalization that eventually causes collapse. Ellison and Corona (1998); Vaze and Corona (1998) and Yin et al. (2004) reported gradual degradation and localized collapse of beams of various cross sections under cyclic bending. Goto et al. (1995) and Corona (2005) reported numerical results on localization of transverse deflection in a periodically supported column undergoing symmetric displacement controlled cycling.

A cyclic loading problem of practical importance to offshore pipelines used to transport hydrocarbons can be outlined as follows. Pipelines buried in a trench (see Fig. 2) are essentially axially restrained. Because of this restraint a temperature change caused by the passage of hot hydrocarbons coupled with high internal pressure can plastically deform the pipe/tube (see Klever et al., 1994). In some cases the compression is high enough to initiate axial wrinkling. Imperfections due to small misalignments at girth welds, heat-affected regions around the welds, hard spots at connections with other equipment etc., can all enhance the onset of wrinkling. During a lifetime of 20–30 years, pipelines experience

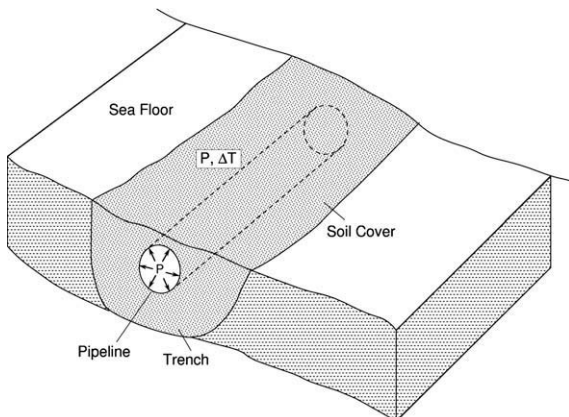


Fig. 2. Schematic of a buried pipeline that develops compression due to change in temperature and internal pressure.

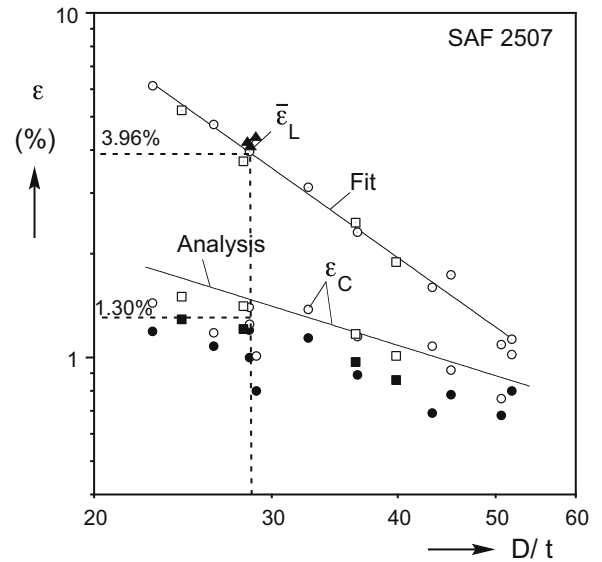


Fig. 3. Critical wrinkling strains (ϵ_c) and average limit strains ($\bar{\epsilon}_L$) vs. D/t from 15 experiments from Bardi and Kyriakides (2006) and three new experiments of $D/t \approx 28.5$.

several startup and shutdown cycles (of the order of hundreds). A question arises as to whether wrinkles formed as a result of such stress risers can grow (ratchet) from the shutdown and startup cycles and if so what are the consequences.

In the present investigation rather than cycling the structure by heat/cool cycles we will consider the following idealized problem that aims to illustrate the interaction of material ratcheting with wrinkling. We will test cylindrical shells with a critical wrinkling strain ϵ_c and a limit strain $\bar{\epsilon}_L (> \epsilon_c)$. Fig. 3 shows a plot of measured values of these two critical average strains as a function of D/t for a super-duplex stainless steel (SAF 2507, from Bardi and Kyriakides (2006)). Thus for example, for shells with D/t of approximately 28.5 that will be used in the present experiments, wrinkling initiates at a strain of about 1.3% and the shell starts to collapse at an average strain of about 4% (exact value influenced by small geometric and other imperfections). The shell will be preloaded to a compressive strain of $\epsilon_c < \bar{\epsilon}_{xmon} < \bar{\epsilon}_L$ (see Fig. 4a) so that wrinkles of small but finite amplitude appear on its surface. The shell will then be cyclically loaded under stress (load) control using the axial stress history shown in Fig. 4b with an amplitude of σ_a about a compressive mean stress of σ_m . These two stress values will be chosen such that the maximum compressive stress in the cycle corresponds to the value at which the specimen was unloaded from during the initial monotonic phase of the loading history. It should be pointed out that these cycle variables determine the rate of material ratcheting. The buried pipeline problem mentioned above involves axial cycling in the presence of internal pressure. Under such loadings the pipe ratchets in both the axial and hoop directions. Investigation of such more complex loadings is left for the future.

2. Experimental

2.1. Experimental set-up and procedures

The cylindrical specimens tested are similar to those used in the monotonic buckling experiments of Bardi and Kyriakides (2006). They were machined out of SAF 2507 super-duplex seamless tube stock (2.375 in (60.3 mm) OD and 0.154 in (3.91 mm) wall). In order to reduce geometric imperfections, both the internal and external diameters of the tubes were machined trying to keep the final

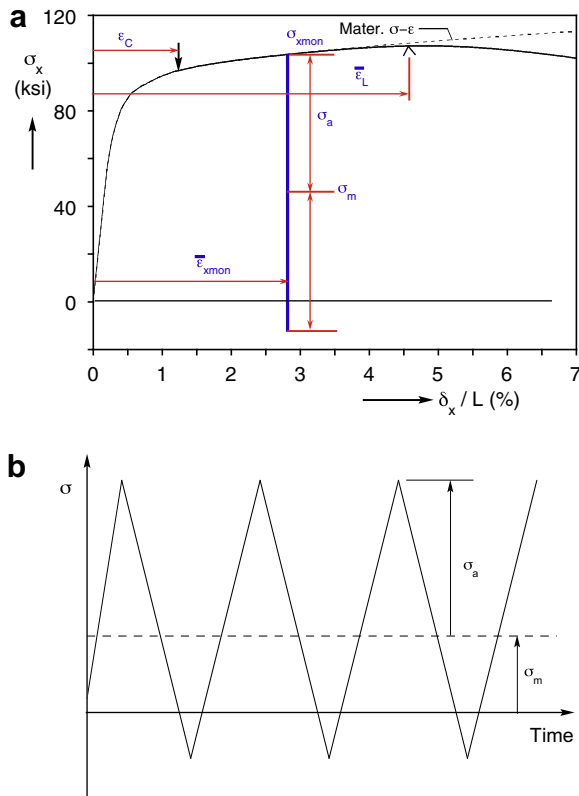


Fig. 4. (a) Monotonic compression stress-shortening response showing the initial pre-staining to $\epsilon_C < \epsilon_{xmon} < \epsilon_L$ and the stress parameters $\{\sigma_m, \sigma_a\}$ of the cycles that follow. (b) Cyclic stress history applied in the experiments.

surfaces parallel with minimum wall eccentricity (typical tolerance ~ 0.001 in– 0.025 mm). The test section has an OD of approximately 2.25 in (57.2 mm), a length of 3 in (76 mm) and a wall thickness of about 0.078 in (1.98 mm). Linear tapers connect the test section to thicker end segments that are left at the as-received diameter (see Fig. 5). The length of the tapers was selected through FE simulations of the test set-up so as to minimize the effect of the thickness discontinuities on the axial stress. The taper geometry chosen shown in Fig. 5 resulted in an overall specimen length of 11 in (280 mm). This choice of specimen geometry implies that the onset and growth of wrinkling was approaching that expected of a long uniform tube.

The specimens were preloaded and cycled in a 225 kip (1 MN) servohydraulic testing machine that can be operated in displacement or load control. The test set up is shown in a scaled schematic in Fig. 6. The thicker parts of the specimen engage custom axisymmetric grips that include *Ringfeder* locking assemblies and solid brass end plugs. A custom extensometer that spans the test section is used to measure its change in length. In some tests the early parts of the axial strain in the test section are also monitored by strain gages.

A scanning device is used to periodically scan the surface of the test section during the test. The device consists of an LVDT displacement transducer mounted on a linear encoder that allows monitoring of the axial position of the transducer. The encoder is mounted on a ring that can rotate concentrically to the test specimen. The angular position is decided by a polar encoder consisting of a photodiode and a graduated black–white tape mounted on the lower grip as shown in Fig. 6. During the cyclic experiments the tube is scanned axially at zero load, at the end of the monotonic part of the loading (i.e., at ϵ_{xmon}), and subsequently during cyclic loading every 10–15 cycles.

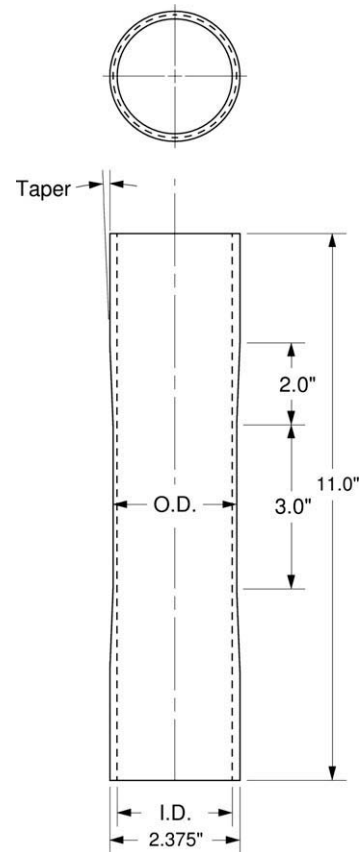


Fig. 5. Geometry of specimens tested.

The initial monotonic loading was conducted at a strain rate of approximately $2 \times 10^{-5} \text{ s}^{-1}$ while the subsequent cycles had periods of 2 min. The tests were monitored via a computer operated data acquisition system that recorded signals from the extensometer, the testing machine displacement transducer, the strain gages and the load cell on a common time base. A second data acquisition system was used to record the axial scans.

Results from three monotonic loading buckling experiments and 10 cyclic experiments will be reported. All test specimens were machined from the same mother tube with approximately the same target OD (D) of 2.25 in (57.2 mm), wall thickness (t) of 0.078 in (1.98 mm), and a gage length (L) of 3.0 in (76 mm). Exact values of these variables that represent the averages of measurements appear in Tables 1 and 2.

2.2. Experimental results – monotonic compression

Fig. 7a shows a representative monotonic stress-shortening response from Exp. CWR10. It exhibits a limit load instability at $\delta_x/L = 4.13\%$. A limited number of axial scans were performed corresponding to the points marked on the response with solid bullets. Fig. 7b shows the radial displacement (w) recorded along the test section from the four scans. The results demonstrate the growth and eventual localization of wrinkles. The number of scans performed was not sufficient to pinpoint the onset of bifurcation as was done in Kyriakides et al. (2005) and Bardi and Kyriakides (2006). Instead, predictions of the critical bifurcation stress and strain values $(\sigma_C, \epsilon_C) = (102.5 \text{ ksi}, 1.48\%)$ developed using the mechanical properties given in Table 3 are listed in Table 1. It should be pointed out that for this tube material and D/t , in the neighborhood of the limit load the tubes tend to switch to a non-axisymmetric buckling mode (usually $n=2$, see Bardi et al.

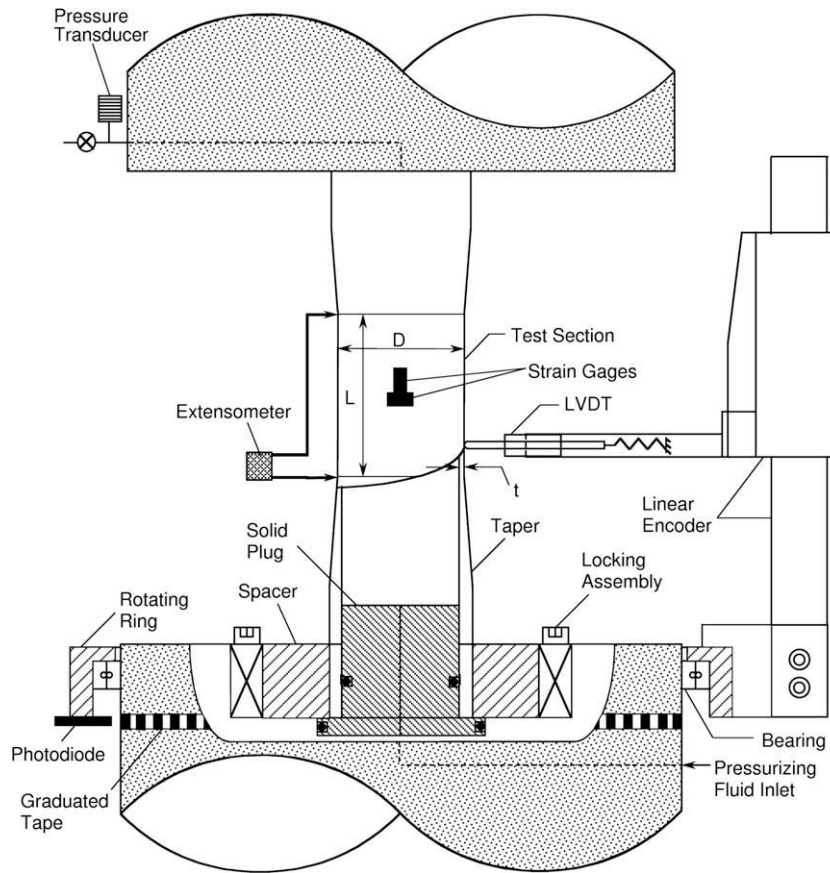


Fig. 6. Scaled schematic of the experimental set-up used.

(2006)), which becomes fully developed and localized if compression is continued well past the limit load.

The results from the other two monotonic loading cases included in the table are similar. The specimen geometry differed slightly from one case to another and each had unique small initial geometric imperfections. The geometric differences cause small differences in the strains at which the wrinkles first appear while the geometric imperfections affect the onset of the limit load instability to the extent shown in the table. The three new limit strains have been added to the results of Bardi and Kyriakides (2006) and are depicted with solid triangular symbols (\blacktriangle) in Fig. 3. They are seen to fall in line with the rest of the data.

2.3. Representative cyclic loading experimental results

Fig. 8a shows the stress–displacement response recorded for one of the cyclic loading experiments (CWR6). This tube was compressed to $\bar{\epsilon}_{xmon} = 2.24\%$ and then unloaded. The maximum stress reached during this part of the test was $\sigma_{xmon} = 108.5$ ksi (748.5

MPa). Fig. 8b shows axial scans of the initial unloaded tube surface and one following plastic deformation from monotonic compression ($N = 0$). By the time the compression level reached $\bar{\epsilon}_{xmon}$, several wrinkles are seen to have formed in the test section. The specimen was then cycled axially in compression under load control about a mean stress $\sigma_m = 37.71$ ksi (260.1 MPa) and an amplitude $\sigma_a = 70.82$ ksi (488.4 MPa) (see Fig. 4b); in other words, the maximum stress in each cycle corresponds to the monotonic unloading stress σ_{xmon} . The specimen immediately starts to ratchet axially as evidenced by the stress–displacement response in Fig. 8a. Fig. 8c shows a plot of the peak displacement (δ_x^p/L) in each cycle vs. the number of the cycle N . Following an initial transient that in this case lasts a few cycles, ratcheting settles to a nearly constant rate. In the neighborhood of cycle 150 (corresponds to an average strain of about 3.4%) ratcheting starts to accelerate eventually growing exponentially. The width of the stress loops in Fig. 8a progressively increases, the peaks of the cycles become rounder and in the last cycle recorded ($N = 182$), the stress is seen to reach a peak and then to decrease before unloading commences.

Table 1
Test specimen parameters and critical variables measured in monotonic axial compression to buckling experiments.

| Exp. No. | D in (mm) | t in (mm) | D/t | $t_{min} - t_{max}$ in (mm) | σ_c^\dagger ksi (MPa) | $\epsilon_c^l\%$ | σ_L ksi (MPa) | $\bar{\epsilon}_L\%$ |
|----------|-------------------|------------------|-------|------------------------------|------------------------------|------------------|----------------------|----------------------|
| CWR10 | 2.2532 (57.23) | 0.0788 (2.00) | 28.57 | 0.0782–0.0796 (1.99–2.02) | 102.5 (707) | 1.48 | 111.20 (767) | 4.13 |
| CWR12 | 2.2516 (57.20) | 0.0778 (1.98) | 28.94 | 0.0772–0.0788 (1.96–2.00) | 103.8 (716) | 1.47 | 114.26 (788) | 4.39 |
| CWR14 | 2.2542 (57.26) | 0.0794 (2.02) | 28.39 | 0.079–0.0798 (2.01–2.03) | 103.6 (715) | 1.50 | 111.28 (767) | 4.25 |

† Bifurcation analysis, $L = 3$ in (76.2 mm).

Table 2
Geometric and material parameters of wrinkling under cyclic loading experiments.

| Exp No. | D in (mm) | t in (mm) | D/t | $t_{\max} - t_{\min}$ in (mm) | σ_{xmon} ksi (MPa) | $\bar{\epsilon}_{xmon}$ (%) | σ_m Ksi (MPa) | σ_a ksi (MPa) | N_c | $\bar{\epsilon}_f$ % | λ/R^\dagger |
|---------|-------------------|------------------|-------|-------------------------------|---------------------------|-----------------------------|----------------------|----------------------|-------|----------------------|---------------------|
| CWR2 | 2.2510 (57.18) | 0.0784 (1.99) | 28.71 | 0.0794/0.0773 (2.02/1.96) | 105.98 (730.9) | 2.43 | 43.38 (299.9) | 62.60 (431.7) | 480 | 4.79 | 0.281 |
| CWR3 | 2.2525 (57.21) | 0.0788 (2.00) | 28.59 | 0.0794/0.0783 (2.02/1.99) | 108.40 (747.6) | 2.29 | 44.25 (305.2) | 64.15 (442.4) | 403 | 4.61 | 0.282 |
| CWR4 | 2.2482 (57.10) | 0.0761 (1.93) | 29.54 | 0.0770/0.0752 (1.96/1.91) | 107.21 (739.4) | 2.18 | 36.88 (254.3) | 70.33 (485.0) | 340 | 4.76 | 0.281 |
| CWR5 | 2.2504 (57.16) | 0.0773 (1.96) | 29.11 | 0.0786/0.0760 (2.00/1.93) | 106.41 (733.9) | 2.30 | 30.57 (210.8) | 75.84 (523.0) | 58 | 4.52 | 0.279 |
| CWR6 | 2.2569 (57.33) | 0.0805 (2.04) | 28.01 | 0.0813/0.0798 (2.06/2.03) | 108.53 (748.5) | 2.24 | 37.71 (260.1) | 70.82 (488.4) | 182 | 4.45 | 0.287 |
| CWR7 | 2.2468 (57.07) | 0.0754 (1.92) | 29.79 | 0.0759/0.0745 (1.93/1.89) | 109.69 (756.5) | 2.34 | 37.71 (260.1) | 71.98 (496.4) | 111 | 4.29 | 0.277 |
| CWR8 | 2.2496 (57.14) | 0.0768 (1.95) | 29.29 | 0.0779/0.0758 (1.98/1.93) | 110.13 (759.5) | 3.00 | 39.80 (274.5) | 70.33 (485.0) | 130 | 4.97 | 0.279 |
| CWR9 | 2.2513 (57.18) | 0.0778 (1.98) | 28.94 | 0.0785/0.0773 (1.99/1.96) | 107.07 (738.4) | 2.61 | 36.74 (253.4) | 70.33 (485.0) | 271 | 5.64 | 0.281 |
| CWR11 | 2.2508 (57.17) | 0.077 (1.95) | 29.23 | 0.0779/0.0761 (1.98/1.93) | 108.31 (747.0) | 2.65 | 37.98 (261.9) | 70.33 (485.0) | 83 | 4.56 | 0.279 |
| CWR13 | 2.2529 (57.22) | 0.0784 (1.99) | 28.74 | 0.0791/0.0775 (2.00/1.97) | 109.63 (756.1) | 2.60 | 39.30 (271.0) | 70.33 (485.0) | 235 | 5.09 | 0.281 |

[†] Calculated values.

This is a sign that the structure is close to collapse and control was lost for part of the cycle.

Fig. 8b shows axial scans taken initially every 30 cycles and in the later parts of the test more often (see cycle numbers in the inset). Wrinkling is seen to localize at an increasing rate at one of the ends of the test section. Indeed we know from experience that this specimen would not be able to survive even one more load cycle, as this most pronounced wrinkle would collapse in the manner

shown in Fig. 12 of Bardi and Kyriakides (2006). The test was thus terminated after cycle 182. Fig. 9 shows a photograph of the specimen after the test. Included in Fig. 8c is the amplitude of this dominant wrinkle (w_{\max}/R) vs. N . The trend of the growth of this variable is similar to that of δ_x^p . Clearly the recorded ratcheting in δ_x^p is partly due to accumulation of material strain and partly due to shortening caused by the growth of the amplitude of the wrinkles, which can be viewed as a structural “damage”. In the early stages of the cyclic history, material ratcheting is the main contributor while in the later parts, during the exponential growth of δ_x^p and w_{\max} , the contribution of wrinkling dominates (under compression there is no reason for material ratcheting to accelerate).

The nature of $\delta_x^p - N$ plot in Fig. 8c is of course reminiscent of a constant load creep curve with N replacing time. Indeed, the results exhibit the instantaneous deformation of a creep curve followed by a *primary* (or *transient*), a *secondary* (or *steady state*) and a *tertiary* regime that here ends with collapse as opposed to rupture in creep. As in creep, the present phenomenon has two mechanisms, material ratcheting and structural degradation in the form of wrinkle growth. But unlike creep where strain hardening and recovery are competing, here the two mechanisms cooperate. The tertiary creep regime is more complex in that it can involve additional mechanisms such as grain boundary separation, internal formation of cracks and voids. In the present phenomenon the wrinkle growth becomes more dominant in the tertiary regime.

In search of a simple measure of the life expectancy of a tube cycled in this manner, we compare collapse under monotonic and under cyclic loads. Thus the horizontal dashed line drawn in Fig. 8c corresponds to the average of the mean strains ($\bar{\epsilon}_{Lmon}$) at the limit loads recorded in the three monotonic experiments. Clearly, in this case the onset of collapse under the cyclic loading history applied occurs very close to the average collapse strain recorded in the monotonic experiments. This important conclusion will be further scrutinized in the light of additional experiments.

Detailed results from a second cyclic experiment are shown in Fig. 10 in order to illustrate the influence of some of the main parameters of the problem on the induced ratcheting and localization. In this case (Exp. CWR4) the specimen was preloaded to the slightly smaller average compressive strain of $\bar{\epsilon}_{xmon} = 2.18\%$ reaching a corresponding stress of 107.21 ksi (739.4 MPa). The specimen was then cycled axially with an amplitude of $\sigma_a = 70.33$ ksi (485 MPa) about a mean stress of $\sigma_m = 36.88$ ksi (254.3 MPa) (see Fig. 10a). The maximum stress of the cycles is again very close to

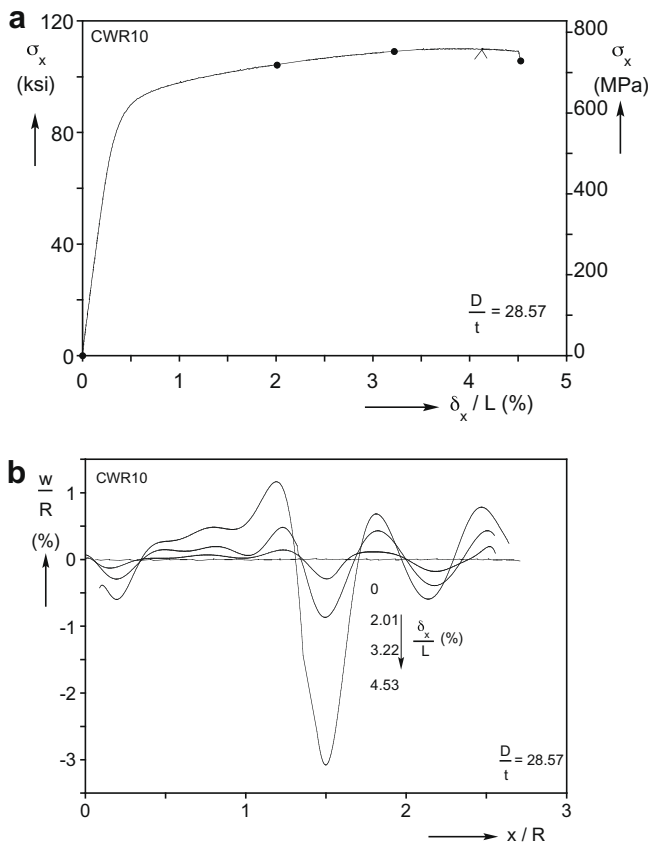


Fig. 7. Typical results from a pure compression test: (a) Recorded axial stress-shortening response. (b) Axial scans showing evolution of wrinkles in test section.

the value reached during the monotonic compression. Although σ_a is about the same as the value in the previous experiment, the peak-to-peak stress level of the cycles is somewhat smaller. Fig. 10b shows that the initial compression wrinkled the tube rather uniformly, but the wrinkles had smaller amplitude than those of CWR6 in Fig. 8b (as will be illustrated using analysis, the amplitude of the initial wrinkles is also influenced by initial imperfections in the tube). This and the somewhat milder stress cycles induce a slower rate of ratcheting as is illustrated in the recorded stress–displacement response in Fig. 10a and in the plot of the cycle peak displacement vs. the number of the cycle in Fig. 10c. The same can be said for the rate of growth of the wrinkle amplitude as illustrated by the w_{\max}/R – N plot included in Fig. 10c. Following a small initial transient, the rate of ratcheting settles to a nearly constant value that is maintained for about 250 cycles. By this time the

amplitude of all wrinkles has grown significantly albeit quite uniformly. Subsequently the rate of ratcheting starts to accelerate and the loops traced become increasingly wider. The rate of growth of the amplitude of the wrinkles also accelerates while simultaneously the deformation localized in one of the ends (see Fig. 10c). The experiment was terminated after cycle 340. Included in Fig. 10c is the average strain at the limit load of the monotonic tests ($\bar{\epsilon}_{Lmon}$). Once more this value is seen to correspond quite well to the cyclic displacement at which the rate of ratcheting and localization are accelerating significantly.

2.4. Summary of cyclic loading experimental results

A total of 10 cyclic experiments like the two described in Section 2.3 were performed in which the main parameters influencing the rate of ratcheting were further evaluated. In the interest of brevity we will mainly report and compare the rate of ratcheting recorded as represented by the net shortening per cycle ($\delta_x^p - N$) response (the stress–strain responses and the evolution of wrinkles will be made available on our website for anyone interested). Thus for example, in Fig. 11 we compare the ratcheting results from six experiments, which had approximately the same average compressive pre-strain of $\bar{\epsilon}_{xmon} \approx 2.3\%$ but with different cycle amplitudes, σ_a , given in the inset. In each case σ_m was chosen so that the maximum stress of the first cycle matched the maximum stress reached during the initial monotonic loading (see Table 2 for details). All trajectories have the characteristic shape of creep curves differing mainly in the extent of the initial transient and that of the steady state. As expected, the effect of σ_a on the rate of ratcheting, represented by the slope of the nearly linear parts of the trajectories, is very significant. Furthermore, in all cases at some point the rate of growth of δ_x^p starts to accelerate becoming exponential. All specimens were cycled up to the point when collapse was eminent at which time the test was terminated.

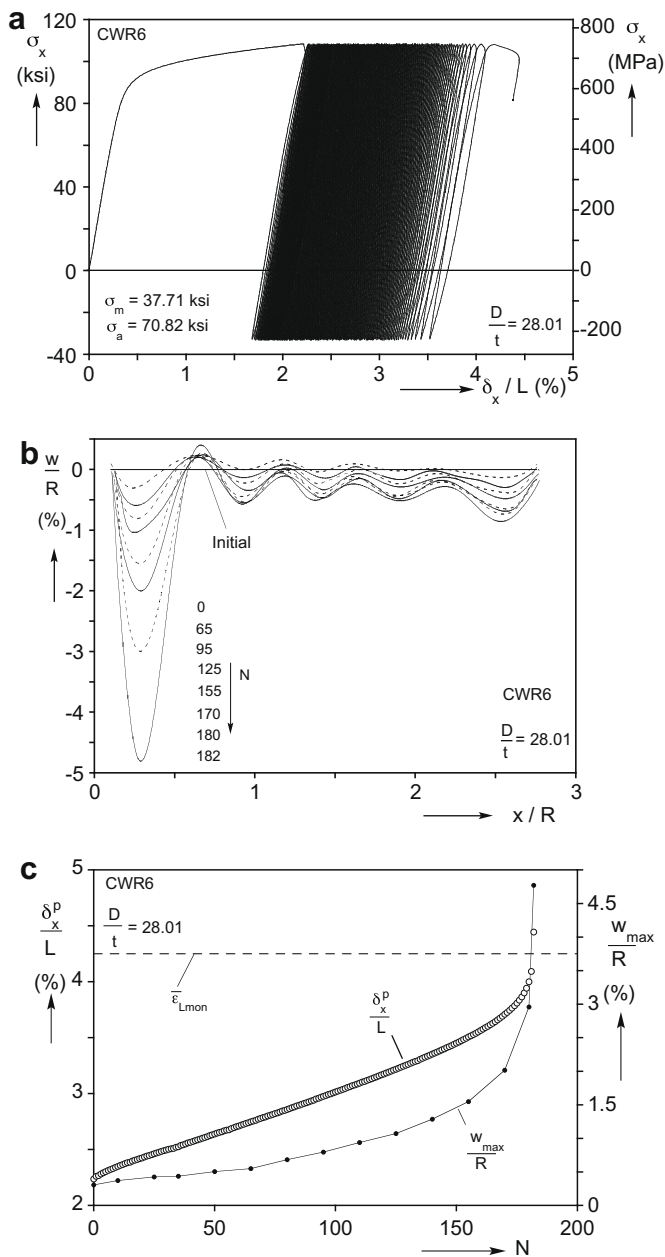


Fig. 8. Results from cyclic loading experiment CWR6. (a) Axial stress–shortening response. (b) Axial scans showing evolution of wrinkles during the cycling. (c) Peak axial displacement per cycle vs. N and corresponding maximum radial displacement in wrinkles.



Fig. 9. Specimen CWR6 at the end of cycling showing wrinkles and localization at one end.

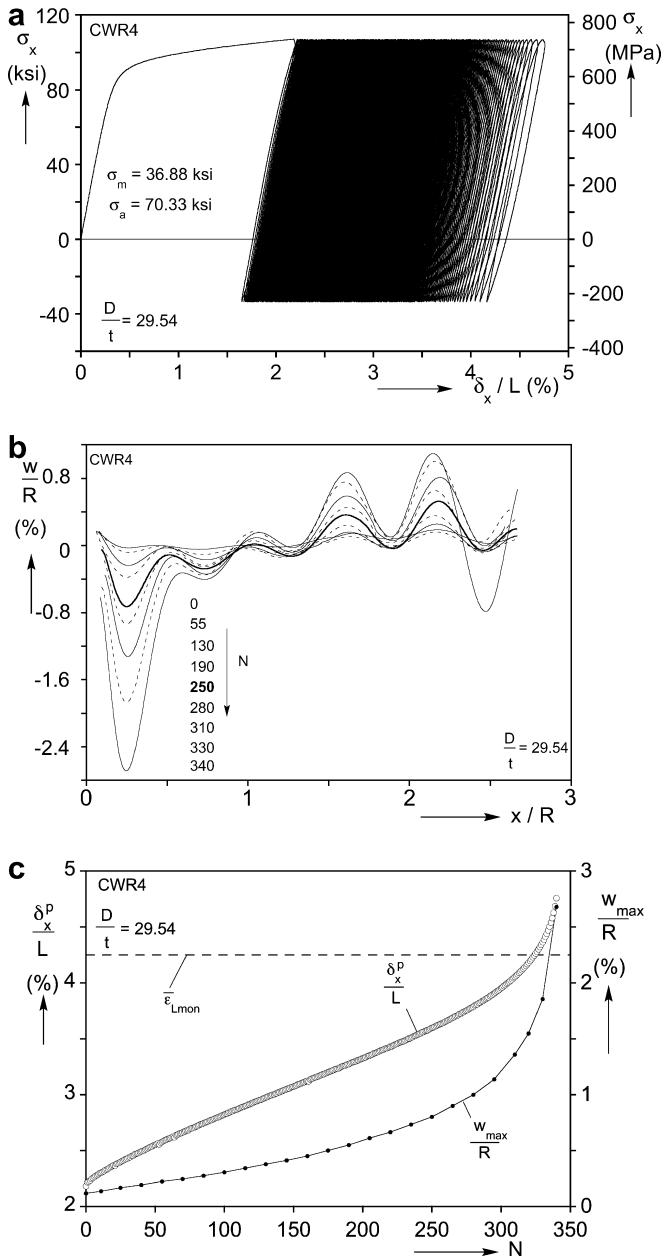


Fig. 10. Results from cyclic loading experiment CWR4. (a) Axial stress-shortening response. (b) Axial scans showing evolution of wrinkles during the cycling. (c) Peak axial displacement in cycles vs. N and corresponding maximum radial displacement in wrinkles.

Included in Fig. 11 is the average strain at the limit loads of the three monotonic loading tests $\bar{\epsilon}_{Lmon}$. This strain level is seen to fall in the part of each trajectory where the rate of ratcheting is in the accelerated rate regime albeit in some cases in the earlier parts and in some in the latter parts of these regimes. This trend confirms the observation made earlier that under cyclic loading the specimens tend to collapse at average strain levels that approximately correspond to that at collapse under monotonic loading. Thus, the average strain under monotonic loading seems to be the maximum strain that the structure can undergo irrespective of how this strain is developed (accumulated). This is a very strong result indeed as it provides a simple means of estimating the life expectancy of such structures under cyclic loads. This observation is reminiscent of a similar one reported in Kyriakides and Shaw (1987) and Corona and Kyriakides (1991) regarding the life span of Al-alloy tubes cyclically bent plastically. This type of cycling causes accumulation

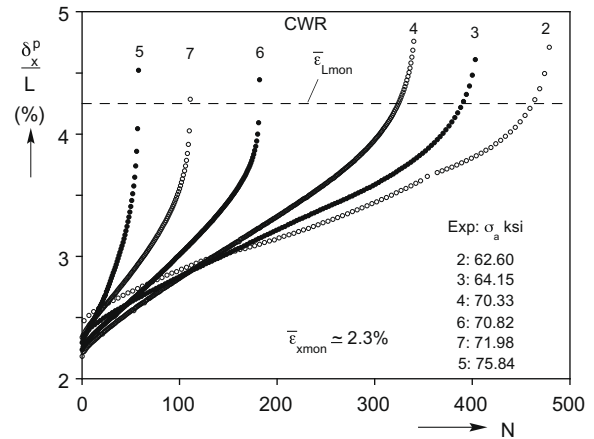


Fig. 11. Peak displacement per cycle vs. N from six experiments with approximately the same initial pre-straining.

of ovalization that eventually leads to collapse. The cycled structure collapses when the accumulated ovalization reaches the value at which it collapses buckling under monotonic bending (similar results were reported recently by Chang and Pan (2009) for stainless steel tubes).

Fig. 12a shows a second set of ratcheting results from experiments in which the specimens were loaded to different levels of strain during monotonic loading while the cycle amplitude was kept constant ($\sigma_a = 70.33$ ksi–485 MPa). In each case the mean stress had to be adjusted slightly in order to match the maximum stress of the cycle with the maximum stress level achieved during monotonic loading (see values in figure inset). Increasing $\bar{\epsilon}_{xmon}$ increases the amplitude of the initial wrinkles as illustrated in Fig. 12b. The $\delta_x^p - N$ results in Fig. 12a show that larger initial wrinkles tend to increase the rate of ratcheting and decrease the number of cycles to collapse. Thus Exp. CWR4 with $\bar{\epsilon}_{xmon} = 2.18\%$ collapsed after 340 cycles while CWR8 with $\bar{\epsilon}_{xmon} = 3.0\%$ reached a critical state after 130 cycles. Once more the rate of ratcheting is seen to accelerate when the accumulated deformation approaches $\bar{\epsilon}_{Lmon}$.

As pointed out earlier, each tube has unique, small initial geometric imperfections that influence the onset of collapse both under monotonic and cyclic loadings. The test specimens were first bored and rimmed on the inside and the outer surface, including the linear tapers, was turned last in an NC lathe. The two step process ends up with very round inner and outer surfaces but minor misalignments in the two setups can result in a small amount of wall eccentricity and misalignment of the axes of the two surfaces. These imperfections were measured manually and their extent manifests in the thickness variations reported in Table 2. Fig. 13 shows the repercussions of variation of imperfections on the rate of ratcheting. Chosen are results from tubes with extreme differences in their imperfections. Fig. 13a shows ratcheting results from three experiments that were compressed to the same average strain of $\bar{\epsilon}_{xmon} = 2.6\%$ and then cycled with the same cyclic stress parameters. Two of the specimens, CWR9 and CWR13, have similar ratcheting responses and a life span of 271 and 235 cycles, respectively. Both of these tubes sustained average strains that are somewhat higher than the 4.25% levels of the monotonic loading tests. The third, CWR11, ratcheted at a much faster rate and lasted only 83 cycles and an average strain that is very close to the level of the monotonic tests that is drawn in the plot with a dashed line. The cause of this difference can be seen in Fig. 13b which shows axial profiles of the wrinkles developed in each tube from the 2.6% shortening induced by monotonic loading. First, the wrinkle profiles are distinctly different in the three

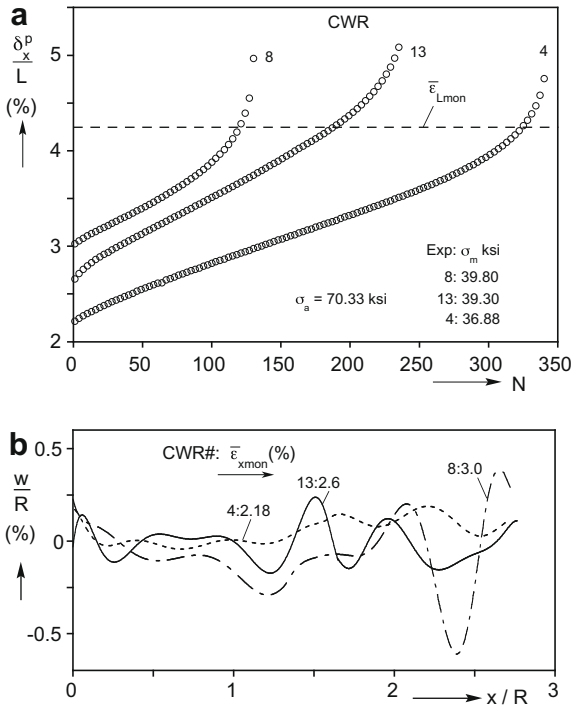


Fig. 12. (a) Peak displacement per cycle vs. N from three experiments with different initial pre-straining and the same stress cycle amplitude. (b) Axial scans of the three specimens showing different amplitude wrinkling caused by the different initial pre-straining.

cases, and second their amplitudes differ. CWR9 has the smallest amplitude, CWR13 somewhat larger while the amplitude of CWR11 is essentially double that of CWR9. The cause of this difference is a somewhat larger eccentricity and inner/outer surface axis misalignment recorded for CWR11.

3. Analysis

3.1. Formulation

The problem of plastic buckling of long circular cylinders under axial compression was fully addressed by Bardi et al. (2006) using an extension of the shell formulation of Yun and Kyriakides (1990). Here we will adopt the same basic formulation, couple it to a cyclic plasticity constitutive model, and use them to analyze the buckling of cylinders under cyclic loads. Because of the challenges placed on the constitutive framework adopted, in this first attempt at the problem strictly axisymmetric buckling will be investigated as this is the dominant mode of buckling for buried offshore pipelines, which typically have D/t values less than 25. Thus we consider a thin-walled circular cylindrical shell with mid-surface radius R , wall thickness t and length $2L$ with small initial axisymmetric imperfections. Sanders' (1963) shell kinematics based on the assumptions of small strains and moderately small rotations are adopted which for axisymmetric deformation reduce to

$$\epsilon_{xx}^o = u_{,x} + \frac{1}{2} w_{,x}^2, \quad \epsilon_{\theta\theta}^o = \frac{w}{R}, \quad \kappa_{xx} = -w_{,xx}. \quad (1a)$$

The strains at any point on the shell are given by:

$$\epsilon_{\alpha\beta} = \left(\epsilon_{\alpha\beta}^o + z\kappa_{\alpha\beta} \right) / (A_\alpha A_\beta)^{1/2}, \quad \text{where } A_1 \cong 1, \quad A_2 \cong 1 + \frac{z}{R}. \quad (1b)$$

For an imperfect structure with imperfection $\bar{w}(x)$ the strains become

$$\epsilon_{\alpha\beta} = \epsilon_{\alpha\beta}(u, w + \bar{w}) - \epsilon_{\alpha\beta}(0, \bar{w}). \quad (1c)$$

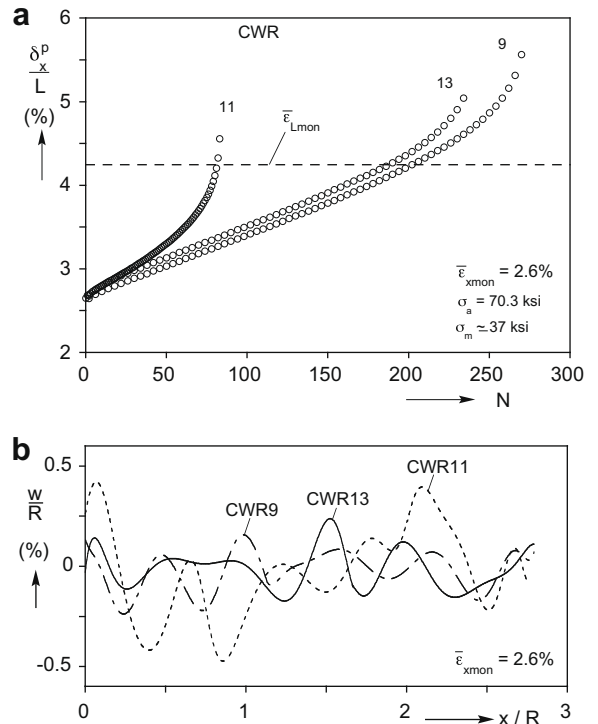


Fig. 13. (a) Peak displacement per cycle vs. N from three experiments with the same initial pre-straining and same stress cycle parameters. The observed difference in the rate of ratcheting and in the average strain at collapse was caused by differences in the amplitude of the wrinkles that develop during the initial pre-straining shown in (b).

Equilibrium will be satisfied through the Principle of Virtual Work (PVW), which in the present setting can be expressed as follows:

$$2\pi R \int_0^L \{ N_{xx} \delta \epsilon_{xx}^o + N_{\theta\theta} \delta \epsilon_{\theta\theta}^o + M_{xx} \delta \kappa_{xx} \} dx = \delta W \quad (2a)$$

where δW is the virtual external work. The membrane and bending moment intensities are given by

$$N_{\alpha\beta} = \int_{-t/2}^{t/2} \frac{A_1 A_2}{(A_\alpha A_\beta)^{1/2}} \sigma_{\alpha\beta} dz, \quad (2b)$$

$$M_{\alpha\beta} = \int_{-t/2}^{t/2} \frac{A_1 A_2}{(A_\alpha A_\beta)^{1/2}} \sigma_{\alpha\beta} z dz, \quad (\alpha, \beta) \text{ not summed.}$$

The evolution of wrinkling during cycling and the development of the anticipated localized collapse are considered by introducing the following initial imperfection to the tube

$$\bar{w} = t \left[\omega_0 + \omega_1 \cos \left(\frac{\pi x}{N\lambda} \right) \right] \cos \left(\frac{\pi x}{\lambda} \right), \quad (3)$$

where 2λ is the wavelength of the axisymmetric buckling mode evaluated as discussed in Kyriakides et al. (2005). The end at $x = N\lambda$ is radially free and symmetry about the specimen mid-span ($x = 0$) is assumed. Thus, the length of the domain considered is $L = N\lambda$ while imperfection (3) introduces an amplitude bias towards $x = 0$. (This is a scheme meant to represent the behavior of a long tube adopted in Bardi and Kyriakides (2006) and found to be effective in reproducing monotonic loading experimental results.)

The problem domain is discretized by adopting the following admissible expansions for the displacements:

$$w = a_0 + \sum_{n=1}^{N_w} a_n \cos \left(\frac{n\pi x}{N\lambda} \right) \quad \text{and} \quad u = b_0 x + \sum_{n=1}^{N_u} b_n \sin \left(\frac{n\pi x}{N\lambda} \right). \quad (4)$$

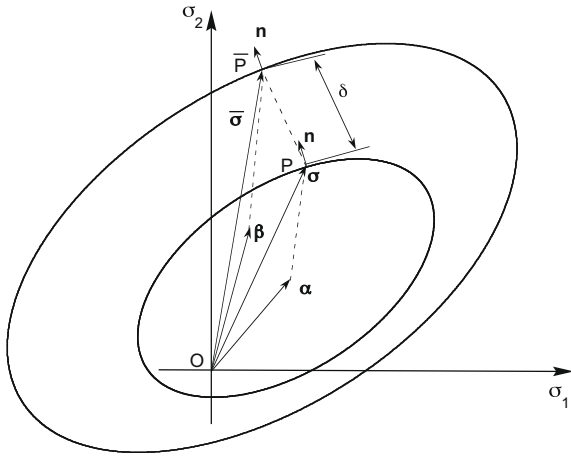


Fig. 15. Yield and bounding surfaces and associated variables of the Dafalias–Popov model.

$$\frac{\partial f}{\partial \sigma} \cdot d\sigma = \frac{\partial f}{\partial \sigma} \cdot d\sigma. \quad (15c)$$

The translation of the BS is coupled to that of the YS as follows:

$$d\beta = d\alpha - dM\mathbf{m}, \quad (16a)$$

where

$$\mathbf{m} = \frac{(\bar{\sigma} - \sigma)}{|\bar{\sigma} - \sigma|} \quad \text{and} \quad dM = \left(1 - \frac{E_b^p}{H}\right) \left(\frac{d\sigma \cdot \mathbf{n}}{\mathbf{m} \cdot \mathbf{n}}\right) \quad (16b)$$

here \mathbf{n} is the unit normal to the YS at the current stress point (see Fig. 15) and E_b^p is evaluated from

$$E_b^p = E_o^p + C_r [(\mathbf{b} \cdot \mathbf{b})^{1/2} - \mathbf{b} \cdot \mathbf{n}]. \quad (17)$$

This modification introduced by Hassan and Kyriakides (1994a,b) allows relaxation or downward shift of the bounds found to be necessary in the prediction of uniaxial ratcheting. When the two surfaces come into contact the BS becomes the active surface and the YS moves so as to remain tangential to it.

Finally the tubes tested exhibit some initial plastic anisotropy (see Kyriakides et al. (2005) and Bardi et al. (2006)) and consequently the yield function becomes:

$$f = \left[(\sigma_x - \alpha_x)^2 - \left(1 + \frac{1}{S_o^2} - \frac{1}{S_r^2}\right) (\sigma_x - \alpha_x)(\sigma_\theta - \alpha_\theta) + \frac{1}{S_o^2} (\sigma_\theta - \alpha_\theta)^2 \right]^{1/2} = \sigma_o. \quad (18)$$

Here $S_r = \sigma_{or}/\sigma_o$, $S_o = \sigma_{o\theta}/\sigma_o$ and $\{\sigma_{or}, \sigma_{o\theta}, \sigma_o\}$ are the yield stresses in the radial, circumferential and axial directions. The bounding surface is also modified in a similar manner becoming

$$F = \left[(\bar{\sigma}_x - \beta_x)^2 - \left(1 + \frac{1}{S_o^2} - \frac{1}{S_r^2}\right) (\bar{\sigma}_x - \beta_x)(\bar{\sigma}_\theta - \beta_\theta) + \frac{1}{S_o^2} (\bar{\sigma}_\theta - \beta_\theta)^2 \right]^{1/2} = \sigma_b. \quad (19)$$

The instantaneous strain increments are then given by

$$\begin{Bmatrix} d\epsilon_x \\ d\epsilon_\theta \end{Bmatrix} = \frac{1}{E} \begin{bmatrix} 1 + Q(2\hat{\sigma}_x - \zeta\hat{\sigma}_\theta)^2 & -v + Q(2\hat{\sigma}_x - \zeta\hat{\sigma}_\theta)(2\eta\hat{\sigma}_\theta - \zeta\hat{\sigma}_x) \\ -v + Q(2\hat{\sigma}_x - \zeta\hat{\sigma}_\theta)(2\eta\hat{\sigma}_\theta - \zeta\hat{\sigma}_x) & 1 + Q(2\eta\hat{\sigma}_\theta - \zeta\hat{\sigma}_x)^2 \end{bmatrix} \times \begin{Bmatrix} d\sigma_x \\ d\sigma_\theta \end{Bmatrix} \quad (20)$$

where

$$\eta = \frac{1}{S_o^2}, \quad \zeta = \left(1 + \frac{1}{S_o^2} - \frac{1}{S_r^2}\right), \quad Q = \frac{1}{4\sigma_o^2} \frac{E}{H}, \quad \hat{\sigma}_x = \sigma_x - \alpha_x, \quad \hat{\sigma}_\theta = \sigma_\theta - \alpha_\theta.$$

3.3. Numerical results

The axisymmetric shell formulation and the nonlinear kinematic hardening constitutive model outlined are now used to simulate several of the cyclic experiments presented. We start with a simulation of CWR6 using the geometric parameters listed in Table 2. The tubes are plastically anisotropic with $\{S_r, S_o\}$ values given below Table 3. Consequently, the critical wrinkle half wavelength was evaluated as in Kyriakides et al. (2005) to be $\lambda = 0.287R$. The imperfection amplitudes $\{\omega_o, \omega_1\}$ were chosen for optimal performance of the model, which in this case were found to be $\{0.09\%, 0.09\%$ (for imperfection sensitivity study see Section 3.4). This tube was pre-compressed to $\bar{\epsilon}_{xmon} = 2.24\%$. The constitutive model parameters used for this part of the loading history come from the initial monotonic stress-strain response of the material and are listed under *Monot.* in Table 3. The parameters used for the stress-controlled cycling come from the stable hysteresis and appear in the same table under *Cyclic*. We note that for monotonic loading a single parameter fit for h in (11b) sufficed, whereas the more elaborate version had to be adopted for fitting the hysteresis.

It is worth pointing out that several of the cyclic fit parameters can influence the rate of ratcheting as well as the rate of growth of the wrinkles, and again these variables were selected for optimal performance of the model. The extent of the influence of the key parameters on the results will be illustrated in the parametric study that follows.

The calculated stress-shortening response is shown in Fig. 16a. Following the initial preloading the model was cycled axially using the cycle variables $\{\sigma_a, \sigma_m\}$ of the experiments. A total of 183 cycles were applied. The characteristics of the calculated response are very similar to those of the corresponding experimental one in Fig. 8a. Fig. 16b shows a plot of the calculated peak displacement in each cycle (δ_x^p/L) vs. N along with the corresponding experimental results. Following an initial transient, the rate of ratcheting of δ_x becomes nearly constant. The rate of ratcheting accelerates around cycle 150 and grows exponentially during the last few cycles very much like in the experiment. Fig. 17a shows plots of the radial displacement along the full domain of $2L = 14\lambda$ for various cycle counts ($x = 0$ represents the plane of symmetry). The amplitudes of the wrinkles are seen to grow with N with the growth of the central wrinkles being more pronounced. Indeed in cycle 183 deformation is seen to have localized around the central wrinkle. The

Table 3
Constitutive model parameters.

| Loading | E Msi (GPa) | E_o^p ksi (GPa) | σ_o ksi (MPa) | σ_b ksi (MPa) | a Msi (GPa) | b | γ | k | C_r |
|---------|---------------|-------------------|----------------------|----------------------|---------------|-----|----------|-----|-------|
| Monot. | 28.2 | 600 | 62.0 | 97.9 | 12.5 | 0 | 0 | 0.1 | 60 |
| | (195) | (4.14) | (428) | (675) | (86.2) | | | | |
| Cyclic | 28.2 | 600 | 47.5 | 114 | 300 | 36 | 3 | 0.1 | 60 |
| | (195) | (4.14) | (328) | (786) | (2069) | | | | |

$$S_o = 1.15, S_r = 0.85$$

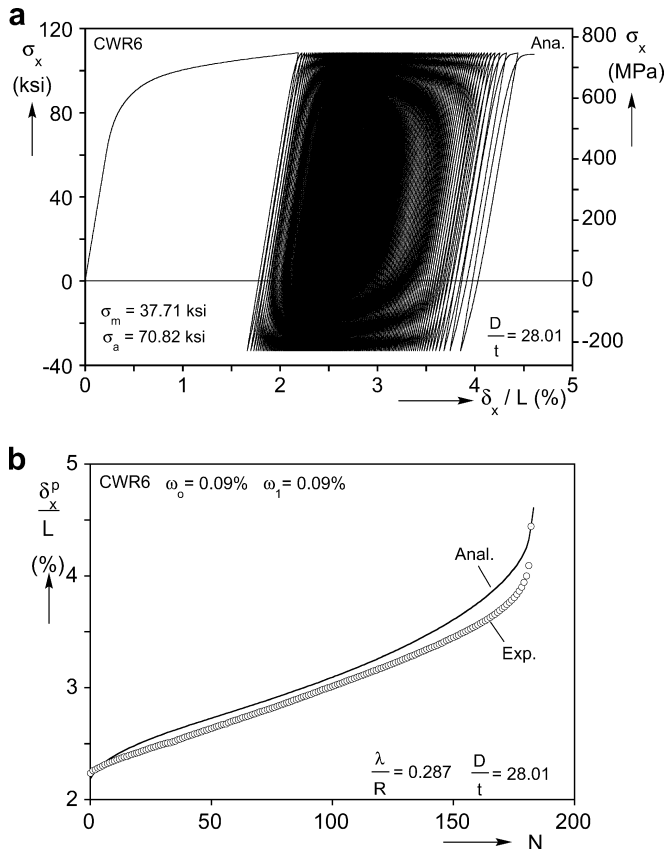


Fig. 16. (a) Calculated axial stress-shortening response for CWR6 and (b) comparison of measured and calculated peak axial displacement per cycle vs. N .

growth of the wrinkles and their localization are also illustrated in Fig. 17b where 3-D renderings of the configuration just before cycling commences ($\bar{\epsilon}_{xmon} = 2.24\%$), one after cycle 150 and a third one after cycle 184 at which the net axial shortening is approximately 6.6% are shown. (Compare Fig. 17a and b with similar ones for monotonic compression shown in Figs. 7 and 8 of Bardi et al. (2006)). The place and nature of the localization are of course different from those of the experiment because of the idealized geometry, imperfection, boundary conditions and axisymmetric nature of the solution adopted. However, overall the model is seen to be

able to reproduce the interaction between material ratcheting and wrinkle growth very well.

A second set of results from a simulation of CWR4 is shown in Fig. 18. In this case the critical wrinkle half-wavelength is slightly different ($\lambda = 0.281R$) but the same imperfection and constitutive model parameters are adopted (Table 3). Overall the simulation reproduces the experimental results shown earlier in Fig. 10 very well. The calculated stress–displacement response in Fig. 18a tracks the experimental one very well and the rate of ratcheting of δ_x^p is seen in Fig. 18b to match the experimental rate very closely.

In view of this success the same imperfection and material parameters were used to simulate all six of the experiments in Fig. 11 that were pre-compressed to $\bar{\epsilon}_{xmon} \approx 2.3\%$. The results from four of the simulations (CWR2, 4, 6 and 7) are summarized in Fig. 19 in the form of $\delta_x^p - N$ ratcheting plots. Despite the very different rates of ratcheting recorded in these experiments the numerical results match the experimental ones very well from the beginning to the end. We suggest that this success over a broad range of stress cycle parameters is caused by similar initial imperfections in the four specimens and simultaneously validates the veracity of the model.

The same imperfection amplitudes were also used to calculate the compressive response under monotonic compression. The response is characterized by a limit load instability in the neighborhood of which deformation localizes as shown in Figs. 6–8 of Bardi et al. (2006). The limit load occurred at $\delta_x/L \equiv \bar{\epsilon}_{Lmon} = 4.48\%$. This value compares with the three experimental values listed in Table 1 that have an average of 4.25%. This average and the prediction are drawn as horizontal lines in Fig. 19. Clearly both fall in the parts of the $\delta_x^p - N$ ratcheting plots where the exponential growth is taking place. This confirms the experimental observation that collapse under monotonic and cyclic loads happens at very similar values of average strain if the tube imperfections are similar.

By contrast, using the same imperfection parameters the corresponding ratcheting results for experiment CWR5 were under-predicted and for CWR3 over-predicted. The most plausible cause of this is small differences between the initial imperfections in these two tubes with those of the other four cases in the group. For a successful reproduction of the experimental rate of ratcheting the imperfection amplitudes $\{\omega_0, \omega_1\}$ for CWR5 had to be both increased to 0.34% whereas for CWR3 they had to be decreased to 0.06% (these results are shown in Fig. 20). This illustrates once more that small initial imperfections can have a significant effect on this type of ratcheting.

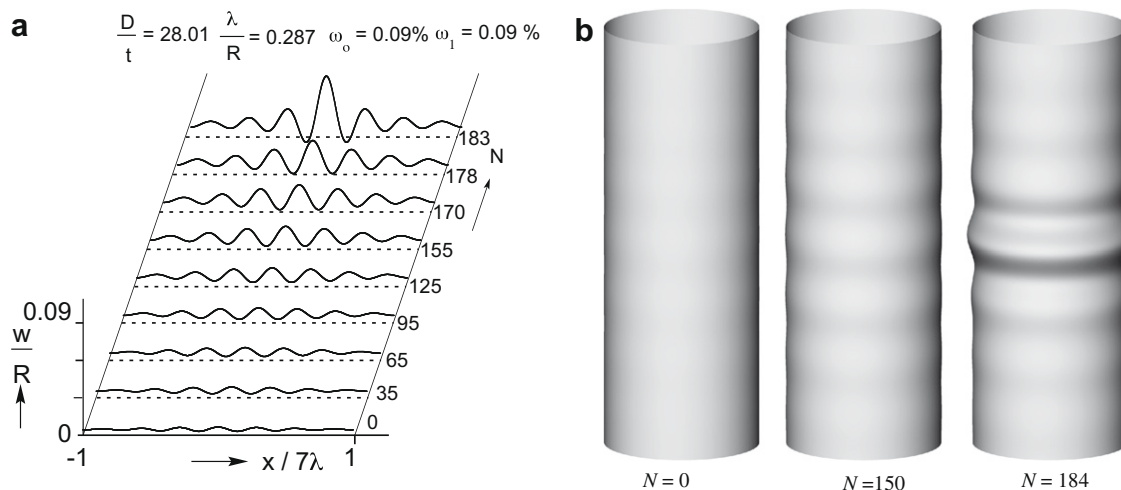


Fig. 17. (a) Calculated radial displacement axial profiles after different number of cycles showing the growth and localization of wrinkles for CWR6. (b) Tube deformed configurations at the onset of cycling, after 150 and 184 cycles.

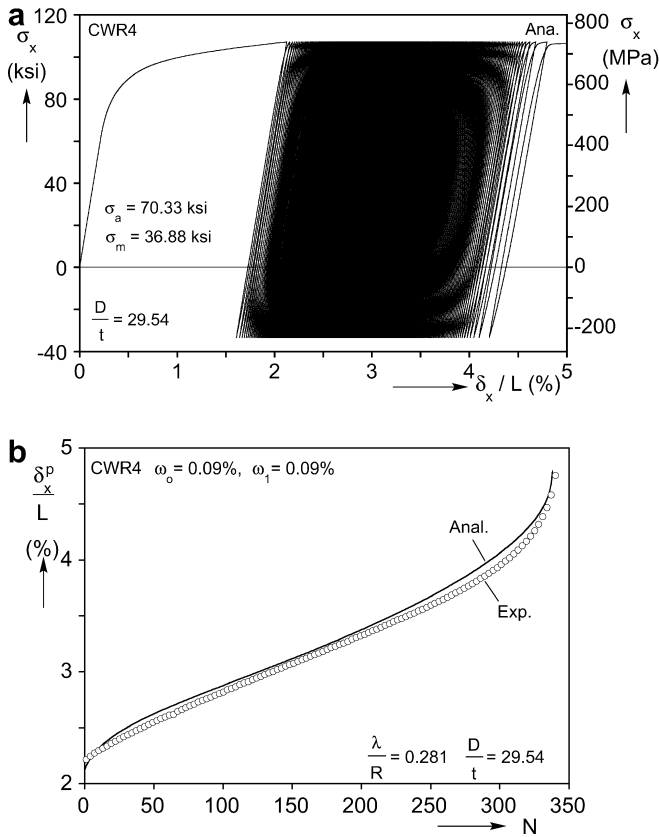


Fig. 18. (a) Calculated axial stress-shortening response for CWR4 and (b) comparison of measured and calculated peak axial displacement per cycle vs. N .

The set of experiments in which the initial compressive strain $\bar{\epsilon}_{xmon}$ was varied were also simulated with the same imperfection and constitutive model parameters. The resultant $\delta_x^p - N$ ratcheting results are compared to the experimental ones in Fig. 21. Although the match between the experimental and predicted results is not perfect in all cases, the overall performance is still very good. Once again, these results indicate that the tubes tend to collapse when a critical amount of deformation or wrinkle amplitude is reached. In the results presented part of the wrinkle growth is introduced by monotonic compression. When this is relatively small then the number of cycles required to reach the critical value is larger,

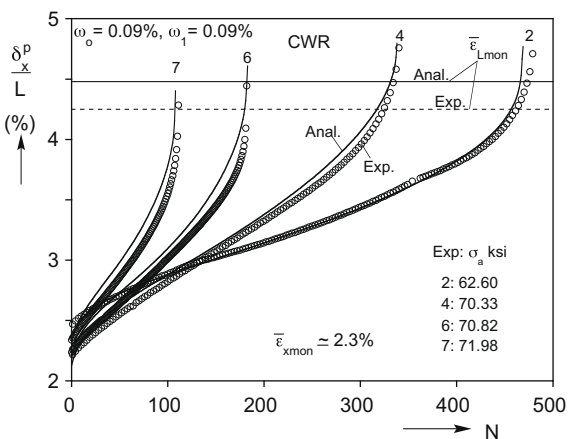


Fig. 19. Comparison of measured and calculated peak displacements per cycle vs. N from four experiments with approximately the same initial pre-straining.

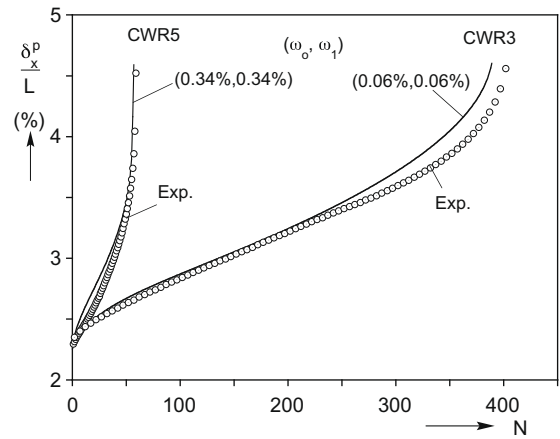


Fig. 20. Comparison of measured and calculated peak displacement per cycle vs. N from two experiments with approximately the same initial pre-straining but different imperfections. The imperfection parameters used in the simulations were different from those used in Fig. 19.

and when it is larger then the critical deformation is reached in fewer stress cycles.

3.4. Sensitivity of ratcheting on problem parameters

The imperfection amplitudes and two of the constitutive model parameters adopted in the simulations discussed in Section 3.3 (see Table 3) were selected for optimal performance of the model in predicting the ratcheting and onset of collapse of most of the experiments performed. We will now treat this set of parameters as the *base case* and demonstrate the effect of individual parameters on the rate of ratcheting by varying them.

3.4.1. Imperfection parameters

Fig. 22a shows $\delta_x^p - N$ ratcheting results for CWR6 for various values of the main imperfection variable ω_o . Here this variable was assigned different values while all other parameters were kept at the basic case levels. This variable affects the rate of ratcheting during most of the loading history. Thus, as ω_o increases from 0.05% to 0.09% to 0.2% the rate of ratcheting is seen to increase with the value 0.09% producing the best agreement with the experimental results. Drawn in the same plot with a dashed line are results for a tube with no imperfections (i.e., $\omega_o = \omega_1 = 0$). In this case

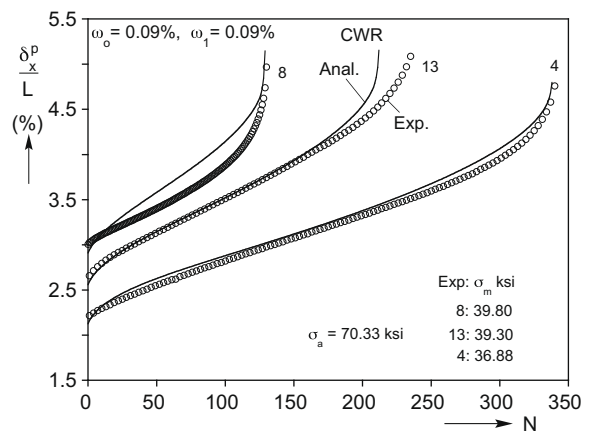


Fig. 21. Comparison of measured and calculated peak displacement per cycle vs. N from three experiments with different initial pre-straining and the same stress cycle amplitude.

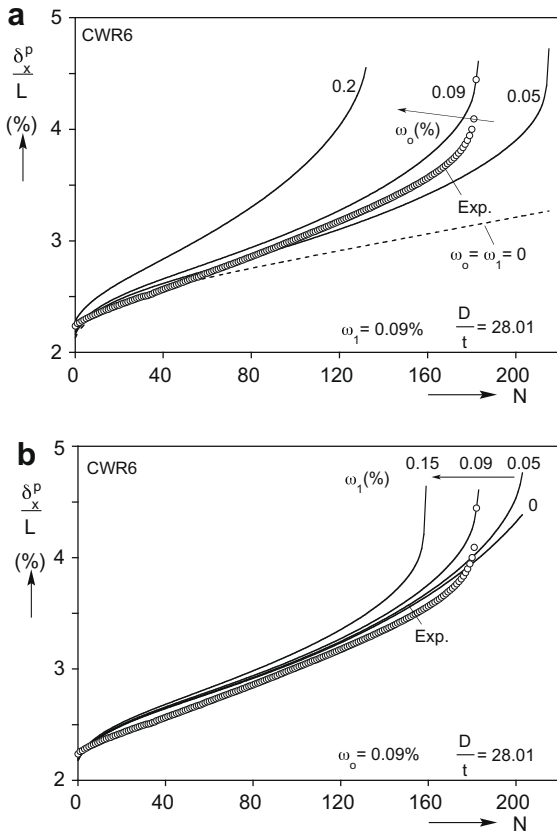


Fig. 22. Effect of imperfection parameters on calculated $\delta_x^p - N$ ratcheting response. (a) Variation of ω_0 and (b) variation of ω_1 .

the tube does not wrinkle or collapse and the accumulation of deformation is purely due to material ratcheting.

Fig. 22b shows similar $\delta_x^p - N$ ratcheting results for different values of the second imperfection parameter, ω_1 , with ω_0 kept at the base value. This variable has relatively small effect on the rate of ratcheting during the part of the history when the wrinkle amplitude is growing at a nearly constant rate. The results clearly show however that this parameter influences significantly the onset of localization; so as ω_1 increases the tube localizes in a fewer number of cycles. The value of 0.09% produces the best agreement with the experimental results.

In Section 2 it was pointed out that the machined tubular specimens used in the experiments had small thickness variations that had some influence on the ratcheting results. In the way of assessing the effect of thickness variations on the rate of ratcheting of our axisymmetric model, the following linearly varying thickness imperfection was introduced to the model:

$$t(x) = t_0[1 - \tau(1 - 2x/L)], \quad \tau = \frac{\Delta t}{t_0} \quad (21)$$

where t_0 is the average thickness and Δt is the amplitude of the variation. Ratcheting calculations were then performed for the loading parameters of CWR6 using three values of τ and the base case problem parameters in Table 3. The results are summarized in the form of $\delta_x^p - N$ ratcheting plots in Fig. 23. Although the thickness variations in the test specimens were not axisymmetric, their amplitudes were typically of the order of 1% of the mean thickness. The results show that for axisymmetric variations of this amplitude this type of imperfection affects mainly the onset of collapse. At much larger amplitudes (e.g., 2.5%) the rate of ratcheting in the steady state part of the simulation is also affected somewhat.

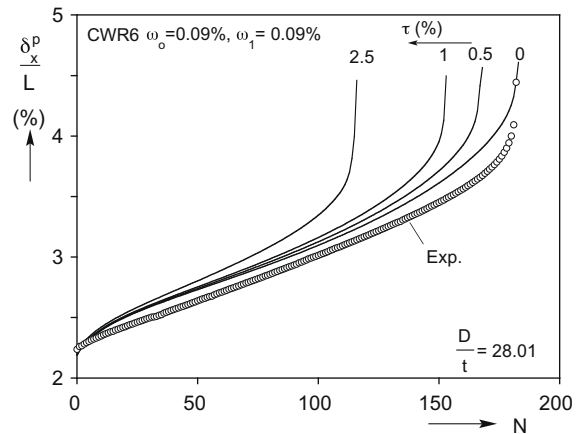


Fig. 23. Effect of thickness variation along the tube length on calculated $\delta_x^p - N$ ratcheting response.

3.4.2. Constitutive model parameters

We now consider two parameters of the constitutive model, C_r and σ_b , that influence material ratcheting and localization of wrinkles. As pointed out in Hassan et al. (1992), when the bound is fixed results in a progressively slower rate of ratcheting as shown in Fig. 24 for $C_r = 0$. Indeed this can eventually lead to shakedown. One way of correcting this performance of the model is to allow the bound to shift downwards, or relax. This is achieved by the introduction of the second term in Eq. (17) with C_r (relaxation coefficient) governing the rate of relaxation (see Hassan and Kyriakides, 1994a,b). The results in Fig. 24 demonstrate that as C_r increases the rate of ratcheting increases. The value of 60 was found to best reproduce the rate of ratcheting in this material.

The size of the bounding surface, σ_b , is another variable that affects the rate of ratcheting. Reducing σ_b decreases the plastic modulus during a stress cycle, increases the final plastic strain, which in turn results in an increase in the rate of ratcheting. The effect of this parameter on the rate of ratcheting is illustrated in Fig. 25 where $\delta_x^p - N$ ratcheting plots for three values of σ_b are compared to the experimental results of CWR6 with all other parameters kept at their base case values. The optimum value adopted in the simulations was $\sigma_b = 114$ ksi (786 MPa).

4. Conclusions

Plastic buckling of circular tubes is characterized by a sequence of instabilities that eventually lead to localized collapse. The tube

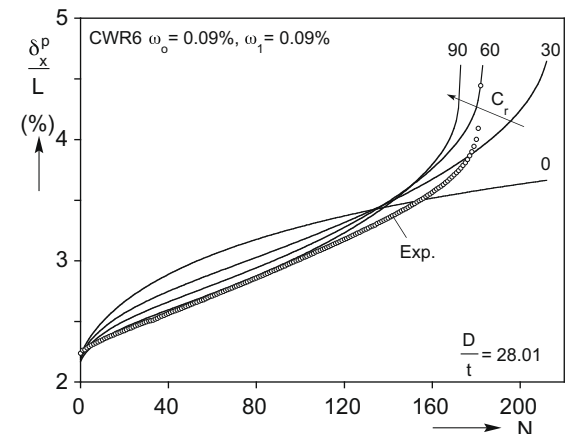


Fig. 24. Effect of relaxation coefficient C_r on calculated $\delta_x^p - N$ ratcheting response.

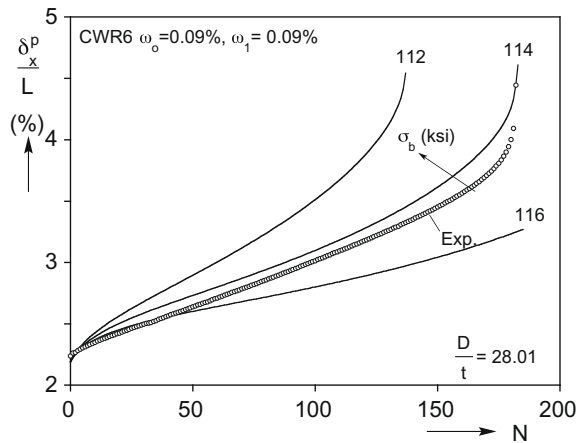


Fig. 25. Effect of bounding surface size σ_b on calculated $\delta_x^p - N$ ratcheting response.

first develops axisymmetric wrinkles, which are initially benign. Under further compression the amplitude of the wrinkles grows, progressively reducing the axial rigidity of the structure and eventually leading to a limit load instability. At this point, with the load dropping, the deformation localizes forming a single bulge that eventually becomes a fold. The onset of wrinkling and the onset of localization can be separated by strain levels of a few percent (separation depends on D/t and material hardening). In this work, we investigated whether a tube that develops small amplitude wrinkles can be collapsed by persistent cycling. To this end, tubular specimens were first compressed to strain levels high enough for mild wrinkles to form; they were then cycled axially under stress control about a compressive mean stress. In a solid, this type of cycling results in material ratcheting. In the present setting, material ratcheting was accompanied by progressive growth of the amplitude of the preexisting wrinkles. The amplitude of the wrinkles covering the test section initially grew uniformly with the number of cycles. This, coupled with the material ratcheting, caused the shortening to grow nearly linearly with the number of cycles applied. When the wrinkles reached a critical amplitude their rate of growth accelerated while simultaneously deformation started to localize, usually at one site. The growth of localization accelerated, with each cycle becoming exponential and resulting in localized collapse of the tube that resembles that seen under monotonic compression. The net shortening- N trajectories traced resemble creep curves with N replaced time. In other words, the trajectories exhibit an initial transient, an extended linear regime and a fast growing one that terminates in collapse. The two mechanisms behind this behavior are material ratcheting and structural degradation in the form of wrinkle growth. Unlike creep the two mechanisms cooperate, with the wrinkle growth being the one responsible for collapse. The following observations can be made from the experiments:

- Collapse under cyclic loading was found to occur when the net shortening or average strain in the tube reached a level that corresponds to the average strain at the load maximum under monotonic loading. This provides a practical way of estimating the life expectancy of a wrinkled tube that is experiencing cyclic loading.
- The number of cycles to collapse is governed first by the level of the initial pre-strain, and second by the mean stress and amplitude of the load cycles.
- As is the case for monotonic loading, initial geometric imperfections can reduce the average strain at failure and the corresponding number of cycles.

The experiments were simulated numerically using nonlinear axisymmetric shell kinematics coupled with the two-surface plasticity model of Dafalias and Popov (1975, 1976) along with modifications of this model recommended for ratcheting applications by Hassan et al. (1992); and Hassan and Kyriakides (1992, 1994a,b). The shell domain analyzed was assigned small initial axisymmetric imperfections with a small bias in order to facilitate localization. The amplitudes of these imperfections were chosen for optimal performance of the model in predicting the rate of ratcheting and the onset of localization. The plasticity model was calibrated to measured stress-strain data of SAF2507 super-duplex stainless steel. Two parameters that were found to influence the calculated rate of ratcheting were also selected for best overall performance of the model.

The numerical model was found to reproduce the material ratcheting, the evolution of wrinkles and their eventual localization very well over the whole range of problem parameters tested. The model also captured the sensitivity to initial geometric imperfections seen in the experiments. Furthermore, it confirmed that collapse under cyclic loadings materializes when the wrinkles reach a critical level, and that the average strain at collapse corresponds to that at the onset of collapse under monotonic loading.

Acknowledgements

The authors acknowledge with thanks financial support of the work received from a consortium of industrial sponsors under the project Structural Integrity of Offshore Pipelines. Preliminary experiments initiated by Ralf Peek aimed to investigate the potential of buckling under cyclic loadings experienced by hot buried pipelines were conducted in 2002–04 by E. Corona and S. Kyriakides.

References

- Armstrong, P.J., Frederick, C.O., 1966. A mathematical representation of the multiaxial Bauschinger effect. Berkeley Nuclear Laboratories, R&D Department, Report No. RD/B/N/731.
- Baird, L., 1911. The elastic limits of iron and steel under cyclical variations of stress. *Phil. Trans. Roy. Soc. London A* 210, 35–55.
- Batterman, S.C., 1965. Plastic buckling of axially compressed cylindrical shells. *AIAA J* 3, 316–325.
- Bardi, F.C., Kyriakides, S., 2006. Plastic buckling of circular tubes under axial compression. Part I: experiments. *Int. J. Mech. Sci.* 48, 830–841.
- Bardi, F.C., Kyriakides, S., Yun, H.D., 2006. Plastic buckling of circular tubes under axial compression. Part II: analysis. *Int. J. Mech. Sci.* 48, 842–854.
- Benham, P.P., 1961. Axial-load and strain cycling fatigue of copper at low endurance. *J. Inst. Met.* 89, 328–338.
- Bushnell, D., 1982. Plastic buckling of various shells. *ASME J. Pres. Ves. Technol.* 104, 51–72.
- Chang, K.-H., Pan, W.-F., 2009. Buckling life estimation of circular tubes under cyclic bending. *Int. J. Solids Struct.* 46, 254–270.
- Coffin Jr., L.F., 1964. The influence of mean stress on the mechanical hysteresis loop shift of 1100 aluminum. *ASME J. Basic Eng.* 86, 673–680.
- Corona, E., 2005. Buckling mode localization in restrained columns under cyclic loading. *ASME J. Appl. Mech.* 72, 620–622.
- Corona, E., Kyriakides, S., 1991. Experimental investigation of the degradation and buckling of circular tubes under cyclic bending and external pressure. *Thin-Walled Struct.* 12, 229–263.
- Dafalias, Y.F., Popov, E.P., 1975. A Model of nonlinearly hardening materials for complex loading. *Acta Mech.* 21, 173–192.
- Dafalias, Y.F., Popov, E.P., 1976. Plastic internal variables formalism of cyclic plasticity. *ASME J. Appl. Mech.* 43, 645–651.
- Ellison, M.S., Corona, E., 1998. Buckling of T-Beams under cyclic bending. *Int. J. Mech. Sci.* 40, 835–855.
- Gellin, S., 1979. Effect of an axisymmetric imperfection on the plastic buckling of an axially compressed cylindrical shell. *ASME J. Appl. Mech.* 46, 125–131.
- Goto, Y., Toba, Y., Matsuoka, H., 1995. Localization of plastic buckling patterns under cyclic loading. *ASCE J. Eng. Mech.* 121:4, 493–501.
- Hassan, T., Kyriakides, S., 1992. Ratcheting in cyclic plasticity. Part I: uniaxial behavior. *Int. J. Plast.* 8, 91–116.
- Hassan, T., Corona, E., Kyriakides, S., 1992. Ratcheting in cyclic plasticity. Part II: multiaxial behavior. *Int. J. Plast.* 8, 117–146.
- Hassan, T., Kyriakides, S., 1994a. Ratcheting of cyclically hardening and softening materials. Part I: uniaxial behavior. *Int. J. Plast.* 10, 149–184.

- Hassan, T., Kyriakides, S., 1994b. Ratcheting of cyclically hardening and softening materials. Part II: multiaxial behavior. *Int. J. Plast.* 10, 185–212.
- Klever, F.J., Palmer, A.C., Kyriakides, S., 1994. Limit-state design of high-temperature pipelines. In: *Proc. 13th International Conference on Offshore Mechanics and Arctic Engineering*, vol. V, Houston, TX, February 1994, pp. 77–92.
- Kyriakides, S., Shaw, P.K., 1987. Inelastic buckling of tubes under cyclic bending. *ASME J. Pres. Ves. Technol.* 109, 169–178.
- Kyriakides, S., Bardi, F.C., Paquette, J.A., 2005. Wrinkling of circular tubes under axial compression: effect of anisotropy. *ASME J. Appl. Mech.* 72, 301–305.
- Kyriakides, S., Corona, E., 2007. *Mechanics of Offshore Pipelines: Volume 1 Buckling and Collapse*. Elsevier, Oxford, UK and Burlington, Massachusetts.
- Kyriakides, S., Corona, E., 1995. *Cyclic Plasticity Routines (CYPROUS)*. Mechanics Report 95/1. Proprietary software.
- Lee, L.H.N., 1962. Inelastic buckling of initially imperfect cylindrical shells subject to axial compression. *J. Aeronaut. Sci.* 29, 87–95.
- Morrow, J.D., 1965. Cyclic plastic strain energy and fatigue of metals. *ASTM STP* 378, 45–87.
- Pilo, D., Reik, W., Mayr, P., Macherauch, E., 1979. Cyclic induced creep of a plain carbon steel at room temperature. *Fatigue Eng Mater Struct* 1, 287–295.
- Sanders Jr., J.L., 1963. Nonlinear theories for thin shells. *Q. Appl. Math.* 21, 21–36.
- Sandor, B.I., 1972. *Fundamentals of Cyclic Stress and Strain*. The University of Wisconsin Press, Madison, Wisconsin.
- Tvergaard, V., 1983a. Plastic buckling of axially compressed circular cylindrical shells. *Thin-Walled Struct.* 1, 139–163.
- Tvergaard, V., 1983b. On the transition from a diamond mode to an axisymmetric mode of collapse in cylindrical shells. *Int. J. Solids Struct.* 19, 845–856.
- Vaze, S., Corona, E., 1998. Degradation and collapse of square tubes under cyclic bending. *Thin-Walled Struct.* 31, 325–341.
- Yin, S., Corona, E., Ellison, M., 2004. Degradation and buckling of I-beams under cyclic pure bending. *ASCE J. Eng. Mech. Div.* 130, 809–817.
- Yun, H.D., Kyriakides, S., 1990. On the beam and shell modes of buckling of buried pipelines. *Soil Dyn. Earthq. Eng.* 9, 179–193.